Available online at www.sciencedirect.com
SCIENCE DIRECT
Coordination Chemistry Reviews 250 (2006) 1497–1513
COORDINATION CHEMISTRY REVIEWS
www.elsevier.com/locate/ccr

Review

Ab initio molecular dynamics simulations of organometallic reactivity

Filippo De Angelis*, Simona Fantacci, Antonio Sgamellotti*

Istituto CNR di Scienze e Tecnologie Molecolari (ISTM), c/o Dipartimento di Chimica, Università di Perugia, I-06123 Perugia, Italy

Received 9 September 2005; accepted 8 February 2006
Available online 6 March 2006

Contents

Abstract

The energetics and reaction mechanism of prototypical organometallic reactions have been investigated by combining static and dynamic density functional calculations, based on the Car–Parrinello method. Such an approach allows us to dynamically sample the potential energy surface of the reactive system at finite temperature, providing useful insights into the reaction mechanism and evidencing the presence of reaction intermediates. Applications of this methodology are presented, ranging from the migratory insertions of carbon monoxide and alkyl-isocyanides into different metal–carbon bonds, to the SiH oxidative addition to $Pt(PH_3)_2$ and the acetylene to vinylidene isomerization in the coordination sphere of a transition metal center.

Keywords: Ab initio molecular dynamics; Car-Parrinello; Organometallic reactivity; DFT calculations

1. Introduction

Tracing the reaction mechanism of complex organometallic reactions represents a challenging field in theoretical and computational chemistry, due to the intrinsic complexity of the potential energy surface involved in the reactive process. Indeed, the presence of a metal center showing different oxidation states and coordination modes coupled to the usually large size of the reactive system, results in a large number of local minima connected by several transition states, which can be hardly sampled by conventional theoretical methods, based on local geometry optimization techniques. Moreover, a description of the interatomic potential which is capable of accurately tackle bond-breaking/bond-forming events is needed, providing, at the same time, accurate reaction energetics at a reasonable computational cost.

* Corresponding authors. Tel.: +39 075 585 5522; fax: +39 075 585 5606.
E-mail address: filippo@thch.unipg.it (F. De Angelis).

0010-8545/$ – see front matter © 2006 Elsevier B.V. All rights reserved.
doi:10.1016/j.ccr.2006.02.008

Density functional-theory (DFT) has become de facto the method of choice for most applications, due to its combination of reasonable scaling with system size and good accuracy in reproducing most ground state properties. Such electronic-structure approach can then be combined with classical molecular dynamics to provide an accurate description of thermodynamic properties and phase stability, atomic dynamics and chemical reactions, or as a tool to sample the salient features of an unknown potential energy surface.

In this context, a powerful tool, which has been only recently widely applied to problems of chemical interest is represented by ab initio molecular dynamics (AIMD) based on the Car–Parrinello method [1]. In a molecular dynamics (MD) simulation the microscopic trajectory of each individual atom in the system is determined by integration of Newton's equations of motion. In classical MD, the system is considered composed of massive, point-like nuclei, with forces acting between them derived from empirical effective potentials. AIMD maintains the same assumption of treating atomic nuclei as classical particles; however, the forces acting on them are considered quantum mechanical in nature, and are derived from an electronic-structure calculation, based, in general on DFT [2]. The approximation of treating quantum-mechanically only the electronic subsystem is usually perfectly appropriate, due to the large difference in mass between electrons and nuclei. The use of Newton's equations of motion for the nuclear evolution implies that vibrational degrees of freedom are not quantised, and will follow a Boltzmann statistics, which is a fully justified approximation only for temperatures comparable with the highest vibrational level in the system considered.

The AIMD approach allows, eventually, to dynamically sample the potential energy surface of the system of interest at finite temperature, providing useful insights into the reaction mechanism and evidencing the presence of eventual reaction intermediates.

In the following, we illustrate how the AIMD methodology can be exploited in combination with "static" DFT calculations of the minima and transition states of prototypical organometallic reactions, to study the hitherto inaccessible dynamical features of these reactions.

The application of AIMD simulations to the study of organometallic reactivity was pioneered by Margl et al. in 1995, who used a combination of static and dynamic DFT methods to investigate the reaction of methane with $Rh(PH_3)_2Cl$ [3a]. This original work has been followed by a series of papers by Ziegler and co-workers [3], by us [4–9] and by many others [10]. This paper is organized as follows: we first briefly describe in Section 2 the theoretical tools and then provide examples of applications. Applications are focused on prototypical organometallic reactions: (i) CO and R–NC migratory insertions into zirconium–carbon bonds and reductive coupling of iminoacyls (Section 3), (ii) CO migratory insertions into nickel–carbon bonds (Section 4), (iii) acetylene to vinylidene conversions in the coordination sphere of a metal center (Section 5) and (iv) SiH oxidative addition to $Pt(PH_3)_2$ (Section 6), finally, the concluding remarks are reported in Section 7.

2. Computational details

We briefly describe in this section some general computational and implementation details which are common to the applications described herein.

2.1. Car–Parrinello calculations

Traditionally, AIMD schemes are based on a plane-wave basis sets and make use of pseudopotentials for the description of core electrons, which results in extremely efficient implementations. The AIMD simulations reported here were performed with the Car–Parrinello method implementing Vanderbilt pseudopotentials [11]. This is a particularly convenient choice since we are dealing with systems containing a single transition metal center surrounded by lighter elements, so significant computational savings can be achieved with respect to conventional norm-conserving pseudopotentials. The applications discussed here were performed with two different parallel implementations [12], based on the original CP code implemented by Pasquarello et al. [13]. For the LDA exchange–correlation functional the Perdew–Zunger parameterization [14] has been used, together with the gradient corrections to the exchange and correlation due to Perdew et al. [15]. Core states are projected out using pseudopotentials. In all cases, the wavefunctions (density) were expanded in plane waves up to an energy cutoff of 25 (2 0 0) Ry, which was found to be an adequate choice in all the investigated cases. Periodic boundary conditions were used within a supercell approach, i.e. by placing the model molecule in cubic boxes of different sizes, allowing, in any case, a minimum of 6.0 Å between repeated images, which is usually sufficiently large to avoid significant coupling between periodic images. The equations of motion were integrated using a time step ranging from 5 (0.146) to 10 a.u. (0.242 fs), with an electronic fictitious mass ranging from 500 to 1000 a.u., depending on the process investigated. Whenever needed, constrained AIMD simulations were performed by means of the SHAKE algorithm [16], employing the slow-growth method [17] in which the constrained parameter is slowly varied as a function of the simulation time, in such a way that the potential energy surface along the considered constraint is dynamically sampled. In these cases, to maintain the system in thermal equilibrium the temperature of the nuclei was controlled by a Nosé thermostat [18], which creates a canonical (NVT) ensemble. Otherwise, a temperature control based on rescaling of atomic velocities was employed. To obtain a thermal distribution of vibrational modes, the temperature was gradually increased by small steps. A point which needs to be stressed is that we perform constrained AIMD simulations only to sample the reactive potential energy surface, without performing any thermodynamical integration along the approximate reaction coordinate.

2.2. Static DFT calculations

For the static DFT optimization of equilibrium geometries and transition states we resort to conventional available quantum/chemistry packages. In particular we use both the Amster-

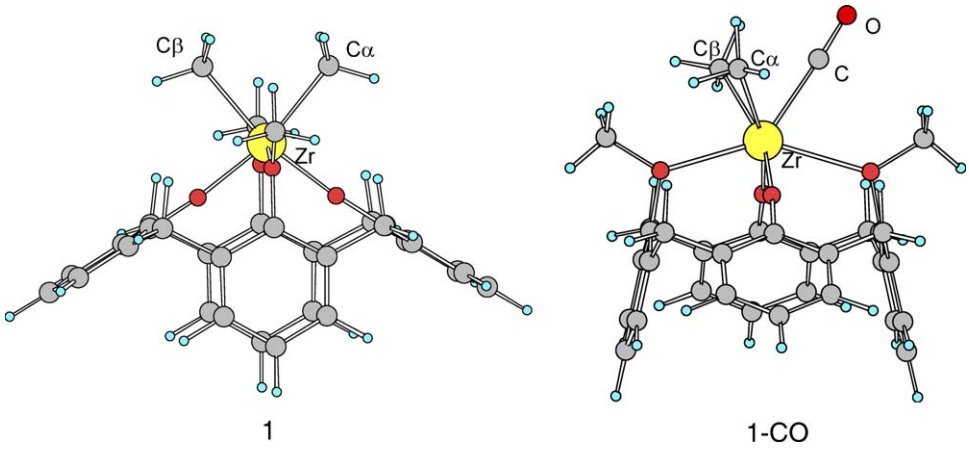

Fig. 1. Optimized molecular structures of the [calix[4]-$(OMe)_2(O)_2ZrMe_2$] complex **1** and of the CO adduct **1**–CO.

dam Density Functional (ADF) program [19] and the Gaussian suite of programs [20]. It has to be noticed that while ADF implements Slater Type Orbitals (STO) basis sets coupled in general to a frozen core approximation, the Gaussian program package makes use of Gaussian Type Orbitals (GTO) and, for heavier transition metal elements, implements pseudopotentials for the description of core electrons. For the ADF calculations we generally used a standard TZVP basis set for the metal atoms and a combination of DZ and DZP for the remaining atoms. For the Gaussian calculations we used a 6-311G* [21] basis set for first transition row metals and a LANL2DZ [22] basis set and pseudopotential for second transition row metals, together with a combination of 6-311G*, 6-31G* [23] and 6-31G basis sets for the remaining atoms. A common feature of all the ADF and Gaussian calculations reported here is the use of the generalized gradient approximation for the exchange–correlation functional, to be consistent with the DFT level of theory employed in AIMD simulations. The Vosko–Wilk–Nusair LDA parameterization [24] was used, including the Becke and Perdew–Wang [25] gradient corrections to the exchange and correlation, respectively. The consistency of the CP and ADF/Gaussian programs was checked in several cases comparing the geometries of different metal complexes for which X-ray data are available, finding a good agreement between the different approaches and experimental data. All the energetics discussed in this review refer to electronic energy differences, without any thermal corrections.

3. Migratory insertions into zirconium–carbon bonds

The migratory insertion of carbon monoxide and isocyanides into metal–alkyl bonds of the early d-block metals has received much attention by synthetic, mechanistic and theoretical points of view [26,27]. Spectroscopic data and structural studies have indicated that isolable CO insertion products contain η^2-acyl groups, where both carbon and oxygen atoms are bound to the metal center, as opposed to an η^1-coordination in which only the carbon is bound to the metal center. Analogously to carbon monoxide, isocyanides insert into early transition metal–alkyl bonds to give η^2-iminoacyl complexes, which undergo insertion of a further alkyl group into the iminoacyl moiety, to generate an η^2-imine, or the uptake of a second isocyanide molecule to give an enediamido [28,29], providing useful synthetic routes to nitrogen-containing organic compounds [28].

In a series of papers, we investigated the reaction mechanism of the migratory insertions of CO and R–NC into the Ti–alkyl and Zr–alkyl bonds of MR_2 units anchored to the prototypical bis-cyclopentadienyl [4] fragment and to a dimethoxy-calix[4]arene dianion, [*p*-Bu^t-calix[4]-$(OMe)_2(O)_2]^{2-}$ [5]. In particular, the reaction of [*p*-Bu^t-calix[4]-$(OMe)_2(O)_2ZrMe_2$], **1** (see Fig. 1), with CO leads to the corresponding η^2-bound acetone, **3** (see Scheme 1) [29]. No intermediates were detected or characterized so that it was assumed [29] that this reaction proceeds via the formation of an η^2-acyl, **2** in Scheme 1, in analogy with what reported for bis-cyclopentadienyl Zr–dialkyl

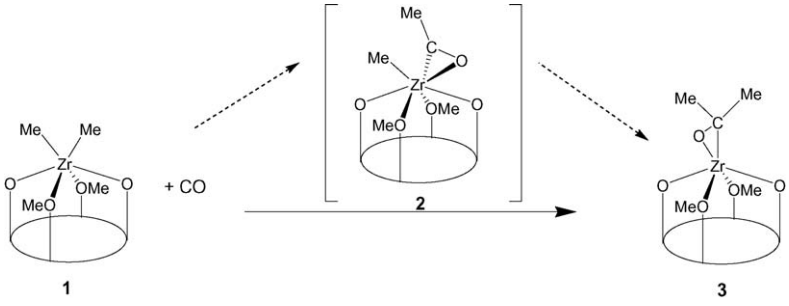

Scheme 1.

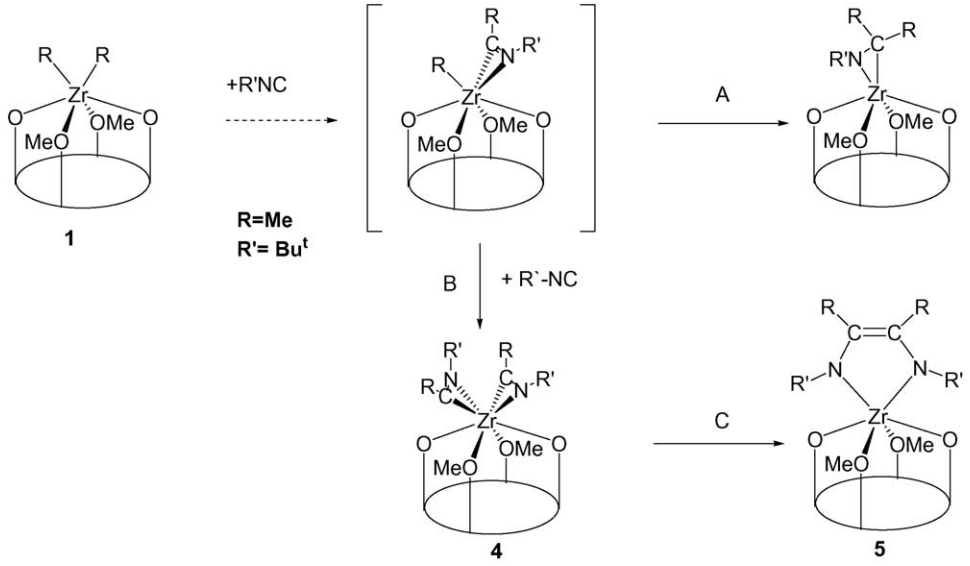

Scheme 2.

complexes [30]. On the other hand, the analogous reaction of **1** with Bu^{t}NC leads to an η^2-imine only at room temperature, see pathway A in Scheme 2, while at low temperature the same process shows the preferential migration of the second alkyl group to an incoming Bu^{t}NC, to give a bis-η^2-iminoacyl complex, **4** [29], see pathway B in Scheme 2. The bis(η^2-iminoacyl) complex **4** is sufficiently stable to be isolated and its mild thermolysis induces intramolecular coupling of the two coordinated iminoacyls with formation of the enediamido product, **5**, see pathway C in Scheme 2. This complex reactivity pattern has been observed for a variety of substrates [31], and can be included into a wider range of important carbon–carbon bond-forming reactions involving the transition metal-assisted reductive coupling of isocyanides.

3.1. CO migratory insertion in [p-Bu^t-calix[4]-(OMe)$_2$(O)$_2$ZrMe$_2$]

In view of the absence of experimental information on the reaction mechanism of the migratory insertion of CO into the Zr–Me bonds of **1**, we performed a "computational experiment" designed to gain insight into the mechanistic features of this reaction. To this aim, we performed AIMD simulations starting from the [*p*-Bu^t-calix[4]-(OMe)$_2$(O)$_2$ZrMe$_2$]–(CO) adduct, **1**–CO in Fig. 1, obtained by coordination of a CO molecule to **1**. The nucleophile coordination to the metal is a common step in both CO and R–NC reactivity, and usually involves small or negligible barriers, mainly due to steric and entropic unfavorable contributions.

We started the dynamics simulation by heating up the structure of **2** to a temperature of 300 K and allowed all the degrees of freedom to evolve naturally for a total time span of 7.5 ps, without applying any constraints to the molecular motion. Hereafter we refer to O, C, C_α and C_β as, respectively, the carbonyl oxygen, the carbonyl carbon, the methyl carbon undergoing the CO insertion and the remaining methyl carbon (see Fig. 1). The CO migratory insertion dynamics can be followed by studying the time evolution of the C_α–C, Zr–C_α, Zr–O, Zr–C_β and C_α–C_β distances. Fig. 2 displays the time evolution of the considered parameters and clearly shows that the reactive CO migration takes place within ca. 0.5 ps, leading to the aforementioned acyl intermediate. Indeed, a fast decrease in the C_α–C distance from ca. 2.4 to 1.5 Å is observed around 0.3 ps, testifying the formation of the new C_α–C bond. The Zr–C_α distance follows an almost complementary trajectory with respect to the C_α–C distance and grows from ca. 2.5 up to 3.7 Å, reflecting the breaking of the Zr–C_α bond. To rationalize whether a possible η^1-acyl structure, **2a**, is formed as a reaction intermediate, we analysed the time evolution of the Zr–O distance in Fig. 2. Clearly, the CO migratory insertion leads initially to an η^1-acyl complex which then rearranges to the corresponding η^2-bound structure, **2b**, as testified by the ca. 1.0 ps delay in the decrease of the Zr–O distance from ca. 3.4 to 2.4 Å, with respect to the formation of the C_α–C bond. Most notably, by allowing the η^2-acyl complex **2b** to evolve freely in time for additional 3.5 ps, we have been able to observe also the formation of the η^2-acetone complex **3**, this process taking place by a methyl to acyl migration from **2b**. Indeed, as it can be noticed from Fig. 2, a fast decrease in the C_α–C_β distance is observed around 4.7 ps indicating the formation of the new C_α–C_β bond, while the Zr–C_β distance shows a coherent increase from ca. 2.4 Å, close to its equilibrium value in **2b**, to 3.3 Å, characteristic of the product **3**, reflecting the detachment of the methyl group from the metal center upon methyl migration. Extracting selected configurations of the various species sampled during the AIMD simulation, we thoroughly characterized the potential energy surface by means of "static" DFT calculations for the overall CO insertion reaction leading to the final η^2-acetone complex **3**. The results, reported in Fig. 3, show that this reaction is characterized by small or negligible energy barriers and by a high exothermicity. The favorable energetics of the CO insertion have allowed us to observe the overall reaction in a reasonable simu-

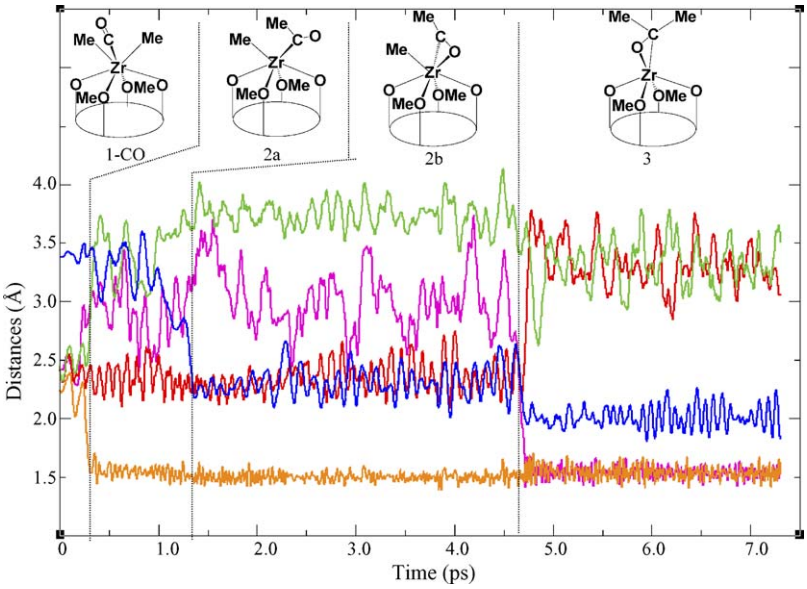

Fig. 2. Time evolution of the C_α–C (orange), Zr–C_α (green), Zr–O (blue), Zr–C_β (red) and C_α–C_β (magenta) distances. Time in ps and distances in Å. Also shown are the structures which are present in the considered time windows.

lation (and computation) time without applying any constraints on the molecular motion.

It is worth noting that sizable differences have been found in the energetics of the corresponding methyl to acyl migration in the $Cp_2Zr(Me)_2(\eta^2\text{-}CH_3CO)$ system, for which an energy barrier of 24.9 kcal/mol has been computed [4a,4b]. The energy barrier difference (22.6 kcal/mol) is remarkable and responsible of the different chemical behavior of the two systems. Indeed, while Zr-bis(cyclopentadienyl) η^2-acyl complexes have been isolated and structurally characterized [30], no Zr-calix[4]arene η^2-acyl could be intercepted [29].

3.2. R-NC migratory insertion in [p-Bu^t-calix[4]-(OMe)$_2$(O)$_2$ZrMe$_2$] and intramolecular coupling of bis(η^2-iminoacyls)

The characterized potential energy surface for the isocyanide migratory insertion into the Zr–methyl bonds of **1** is reported in Fig. 3 together with that for the CO insertion for a direct comparison. As it can be noticed the two insertion reactions show similar characteristics, even though the isocyanide insertion is characterized by slightly higher energy barriers and a smaller overall exothermicity, see Fig. 3. The dynamics of the isocyanide

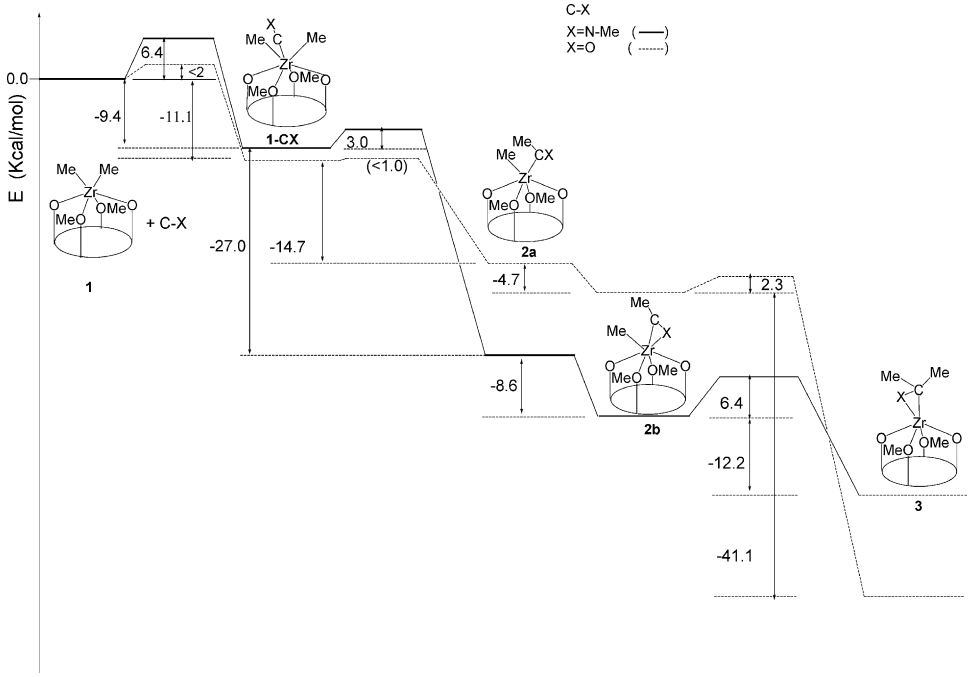

Fig. 3. Energetics of the CO (dashed lines) and R–NC (solid lines) migratory insertion reactions.

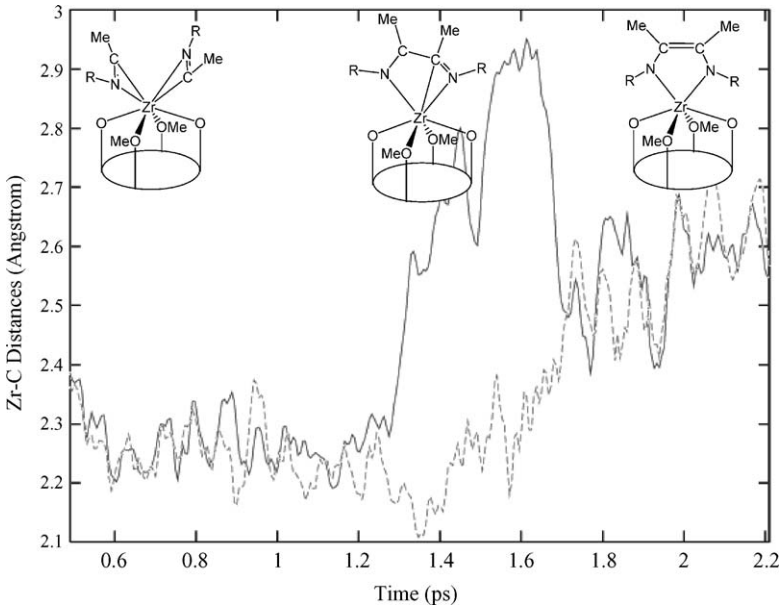

Fig. 4. Time evolution of the two iminoacyl Zr–C bond distances, for the time span going from 0.5 to 2.2 ps. Time in ps and distances in Å.

insertion is detailed in ref. [5b] and compared to that for CO insertion in ref. [5c] and we address the reader to these references for further details.

Here we focus, instead, on the intramolecular coupling of the two iminoacyl units in the bis(η^2-iminoacyl) complex **4** in Scheme 2. For the iminoacyl coupling in bis(η^2-iminoacyl) Zr–di-aryloxide complexes Durfee et al. [28b] proposed a synchronous disrotatory mechanism based on the isolation and X-ray characterization of several bis(η^2-iminoacyls) all showing a head-to-tail arrangement of the two coordinated iminoacyl units [28c]. DFT calculations by Hardesty et al. [32] on a simplified bis(η^2-iminoacyls)–Zr(OH_2) complex essentially confirmed this mechanism. On the other hand, on the basis of AIMD simulations, we recently proposed an alternative mechanism for the bis(η^2-iminoacyl) coupling on di-aryloxide and calix[4]arenes Zr-complexes [5d].

Constrained AIMD simulations were performed on the bis($\eta^2$2-iminoacyl) complex **4**. Starting from its optimized geometry, the system was equilibrated for 1.0 ps at 350 K. Thereafter, the iminoacyl intramolecular C–C distance, assumed as an approximate reaction coordinate (RC), was constrained to vary in the range 3.3–1.4 Å during a total time span of 1.8 ps, allowing all the other degrees of freedom to follow their natural evolution. After 1.8 ps the constraint on the C–C distance was removed, allowing the system to evolve naturally in time for additional 0.4 ps. The iminoacyl C–C distance represents a natural choice for the approximate RC, since its variation connects the reagent and product basins, accounting for the intramolecular formation of the new carbon–carbon bond. The iminoacyl coupling reaction can be followed by studying the evolution of the two iminoacyl Zr–C distances as a function of the simulation time. Fig. 4 displays the time evolution of the two Zr–C distances, and surprisingly shows that the intramolecular carbon–carbon bond formation takes place via an asynchronous reaction mechanism. Indeed, after 1.3 ps (corresponding to a value of the iminoacyl C–C distance of 1.87 Å), one Zr–C distance exhibits a wide oscillation up to 2.95 Å, indicating the detachment of the carbon atom of one iminoacyl unit from the metal center. On the other hand, the other Zr–C distance keeps on oscillating around its equilibrium value in the bis(η^2-iminoacyl) reagent up to 1.6 ps, and only after this time it increases to a value close to 2.5 Å, reaching the value of the other Zr–C distance. We notice that the asynchronous reaction mechanism outlined above is not determined by the particular choice of the approximate RC, since in principle a synchronous reaction pathway might well take place following the system evolution along the same RC. Extracting selected configurations from the AIMD simulations we have been able to optimize the geometry of the transition state connecting the bis(η^2-iminoacyl) **4** to the enediamido product **5**. The optimized transition state structure shows an η^2-coordinated iminoacyl being attacked by a decoordinated iminoacyl unit (see Fig. 4), and is computed to lie 21.2 kcal/mol above the starting bis(η^2-iminoacyl) complex, in good agreement with the experimental activation enthalpy of 25.4 kcal/mol [29]. Most notably, we calculate the transition state for the synchronous coupling reaction, located on the C_2 potential energy surface, to be 20.1 kcal/mol higher than that for the asynchronous reaction pathway, confirming the validity of the proposed reaction mechanism.

4. Migratory insertions into nickel–carbon bonds

The migratory insertion of carbon monoxide into nickel–carbon bonds is a fundamental step of important catalytic processes such as the Reppe carbonylation of acetylene to acrylic ester [33,34] and the copolimerization of carbon monoxide and olefins [35,36]. In the Reppe carbonylation process, the CO inserts into a nickel–alkenyl bond, while in the copolimerization of carbon monoxide and olefins a CO molecule is inserted into a nickel–alkyl bond. These migratory insertion reactions are

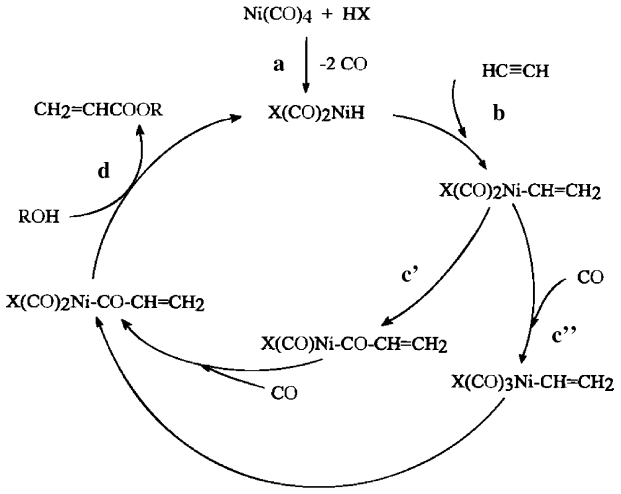

Scheme 3.

members of a larger class of migratory insertion reactions that constitute key steps of transition metal catalyzed carbon–carbon bond-forming reactions [37].

The Reppe carbonylation of acetylene to acrylic ester on nickel carbonyl involves five steps: (a) the oxidative addition of HX to nickel carbonyl, (b) the addition of acetylene to the metal and its subsequent insertion into the Ni–H bond, (c′) the migratory insertion of CO into the Ni–CH=CH_2 bond followed by the coordination of a further CO molecule or (c″) the coordination of CO to nickel followed by the CO insertion into the nickel–vinyl bond and (d) the addition of a water molecule, with the elimination of acrylic acid (see Scheme 3). We report here the results of AIMD simulations on the CO migratory insertions of steps c′and c″[6a,6b]. Results for the overall thermodynamics and kinetics of the full catalytic cycle are reported in ref. [6b].

The reaction pathways for steps c′and c″are schematically represented as A and B, respectively, in Scheme 4. The starting reactant for both pathways A and B is the $Cl(CO)_2Ni$–CH=CH_2 vinyl complex, **6** in Scheme 4, for which we found a *trans*-square-planar arrangement to be slightly favored (0.5 kcal/mol) over the corresponding *cis* isomer. We therefore first performed AIMD simulations on pathway A, and heated up the structure of the more stable *trans*-**6** isomer to a temperature of 600 K. The dynamics of the CO insertion from **6** can be followed by studying the time evolution of the distance between the carbonyl group and the metal attached carbon of the vinyl moiety (C1–C2), and the metal–vinyl distance (Ni–C2). The time evolution of the considered parameters are reported in Fig. 5a, from which it is clear that the migratory insertion takes place within 0.8 ps, as testified by the sudden decrease in the C–C distance from ca. 2.8 to 1.5 Å and the concomitant increase in the Ni–C distance, which reflect, respectively, the formation of the new C–C bond and the breaking of the Ni–C bond. In Fig. 5b, we report the time evolution of the carbonyl–nickel–vinyl (C1–Ni–C2) and of the carbonyl–nickel–carbonyl (C1–Ni–C3) angles. The closure of the C1–Ni–C2 angle from ca. 100° to 30° taking place within 0.8 ps confirms the achievement of the migratory insertion, while the decrease of the C1–Ni–C3 angle

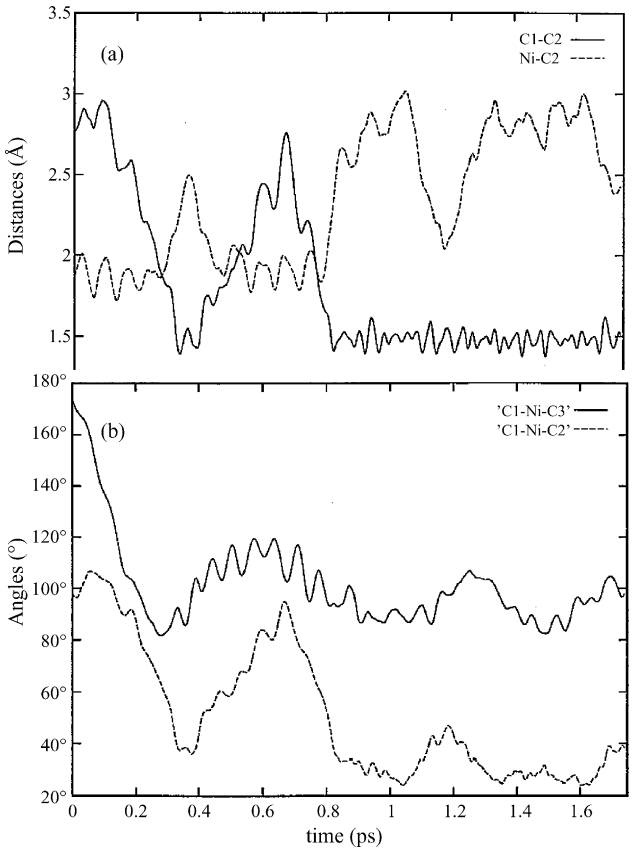

Fig. 5. (a) Time evolution of the C–C (solid line) and Ni–C (dashed line). Time in ps and distances in Å. (b) Time evolution of the C–Ni–C (carbonyl–carbonyl) (solid line) and C–Ni–C angle (vinyl–carbonyl) (dashed line). Time in ps and angles in degrees.

from ca. 180° to 90° taking place around 0.4 ps shows that the migratory insertion is preceded by the conversion of the *trans*-**6** isomer into the corresponding *cis* isomer, the two isomers being characterized by C1–Ni–C3 angles of ca. 180° and 90°, respectively. These results suggest that the CO insertion from the *cis*-**6** isomer seems to be favored over the corresponding reaction from the more stable *trans*-**6** isomer. Indeed, optimization of the transition states for the CO insertion from the *trans* and *cis*-**6** isomers led to energy barriers of 9.6 and 2.2 kcal/mol, respectively, confirming that the pathway passing through the *cis*-**6** isomer is kinetically favored. Pathway A, leading to the trigonal $Cl(CO)Ni$–$COCH=CH_2$ product **7** in Scheme 4, is calculated to be moderately exothermic, by 3.8 kcal/mol.

We then considered pathway B, in which an external CO molecule is first coordinated to **6**, leading to a pentacoordinated trigonal bipyramid (TBP) complex, **8** in Scheme 4. The CO coordination to **6** was calculated to be favored by 8.1 kcal/mol, so that this process is likely to happen in the experimental conditions. The carbonyl insertion might then take place from this species by direct attack of a CO group to the α carbon of the vinyl group. Among the four possible TBP isomers of **8**, we calculate the one with axial chlorine and vinyl groups **8a** to be more stable than that with axial vinyl and carbonyl **8b** by only 1.9 kcal/mol (see Fig. 6), while the isomer with axial chlorine and car-

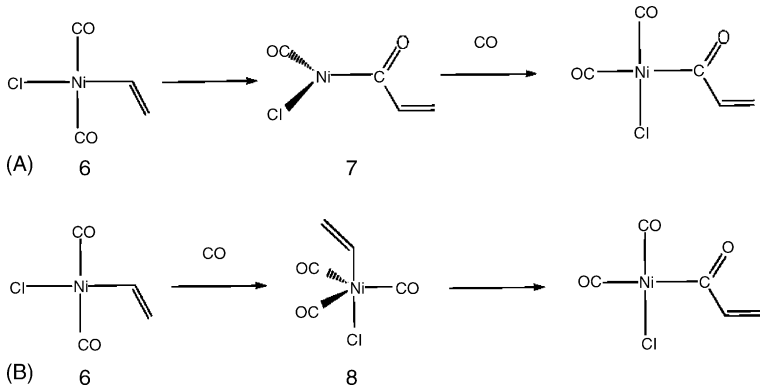

Scheme 4.

bonyl and that with both carbonyls in axial position are not stable.

We therefore started the AIMD simulation by heating up the structure of the more stable TBP **8a** isomer to a temperature of 600 K. Also in this case, the CO insertion reaction can be followed by studying the time evolution of the C–C distance between the carbonyl group and the metal attached carbon of the vinyl moiety. Fig. 7a displays the variation of the considered parameter as a function of the simulation time and clearly shows that the reactive CO migration takes place within ca. 6 ps, as testified by the fast decrease observed in the C–C distance from ca. 2.6 to 1.5 Å, which reflects the formation of the new carbon–carbon bond. Further insight into the dynamics of the CO migration can be gained by analyzing the time evolution of the Cl–Ni–C (vinyl) and C–Ni–C (carbonyl–carbonyl) angles. The considered parameters are reported in Fig. 7b, from which we see that a conversion between the TBP **8a** and **8b** isomers takes place within 1.5 ps, and therefore prior to the migratory insertion event. Indeed, the Cl–Ni–C angle is 175° in the **8a** isomer, where the Cl and vinyl groups occupy the axial positions, while it decreases to ca. 90° in the isomer **8b** where a CO group replaces the Cl ligand in the axial position. Moreover, from Fig. 7b we see that the exchange between axial and equatorial ligands takes place together with a crossing of two equatorial ligands and formation of a pyramidal intermediate, as suggested by the similar decrease observed in the C–Ni–C (carbonyl–carbonyl) Cl–Ni–C angles. Transition state search starting from complex **8a** led to an energy barrier of 5.7 kcal/mol for the carbonyl insertion, with quite a high exothermicity (14.4 kcal/mol). Due to the small energy difference between **8a** and **8b**, we computed also the transition state for CO insertion starting from complex **8b**, finding an energy barrier of 4.1 kcal/mol. Thus the reaction pathways from isomers **8a** and **8b** are both energetically accessible, even though reaction from the former is slightly kinetically favored.

A comparison between the energetics of pathways A and B is reported in Fig. 8, and shows that the latter pathway is energetically favored, since its transition state is 4.5 kcal/mol (8.1 + 2.1 − 5.7) lower than the transition state of pathway A. Indeed, even though CO migration from **6** shows a lower energy barrier compared to migration from **8**, 2.1 kcal/mol versus 5.7 kcal/mol, the favorable contribution due to CO coordination to **6** renders pathway B favored.

It is worth noting that we found a five-coordinate pathway to be favored over a four-coordinate one also in the CO and olefin copolymerization catalyzed by the $[(L–L)Ni(CH_3)(solv)]^+$, L–L= dppp and *o*-MeO-dppe, cationic Ni(II) complex [6c]. In this system, the coordinated CO molecule inserts into a nickel–alkyl bond, rather than in a nickel–alkenyl bond as in the Reppe carbonylation. The calculated energetics for the four and five-coordinate pathways in this system, obtained by a combination of AIMD simulations and "static" DFT calculations, show that also in this case the CO coordination energy to the initial four-coordinated catalyst is the driving force which renders the five-coordinate pathway favored.

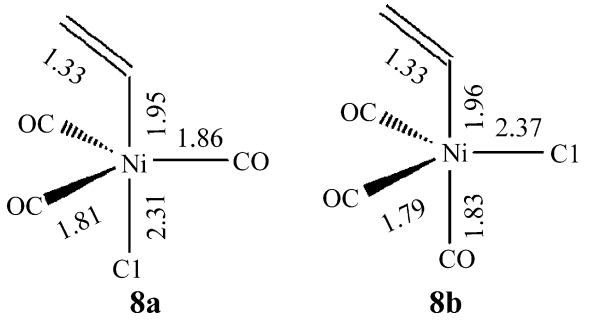

Fig. 6. Optimized geometrical structures of the two TBP isomers of complex **8**. Distances in Å.

5. Acetylene to vinylidene isomerizations

The reactivity of unsatured hydrocarbons on transition metal centers is a topic of great interest in both homogeneous and heterogeneous catalysis [38]. In particular, the acetylene–vinylidene rearrangement in the coordination sphere of a transition metal has attracted considerable interest [39]. While the formation of vinylidene from free acetylene is strongly endothermic (44–47 kcal/mol) [39], the relative energies of the two isomers change dramatically in the coordination sphere of transition metals. Metal vinylidenes are stable complexes and may be more stable than the corresponding acetylene isomers [40].

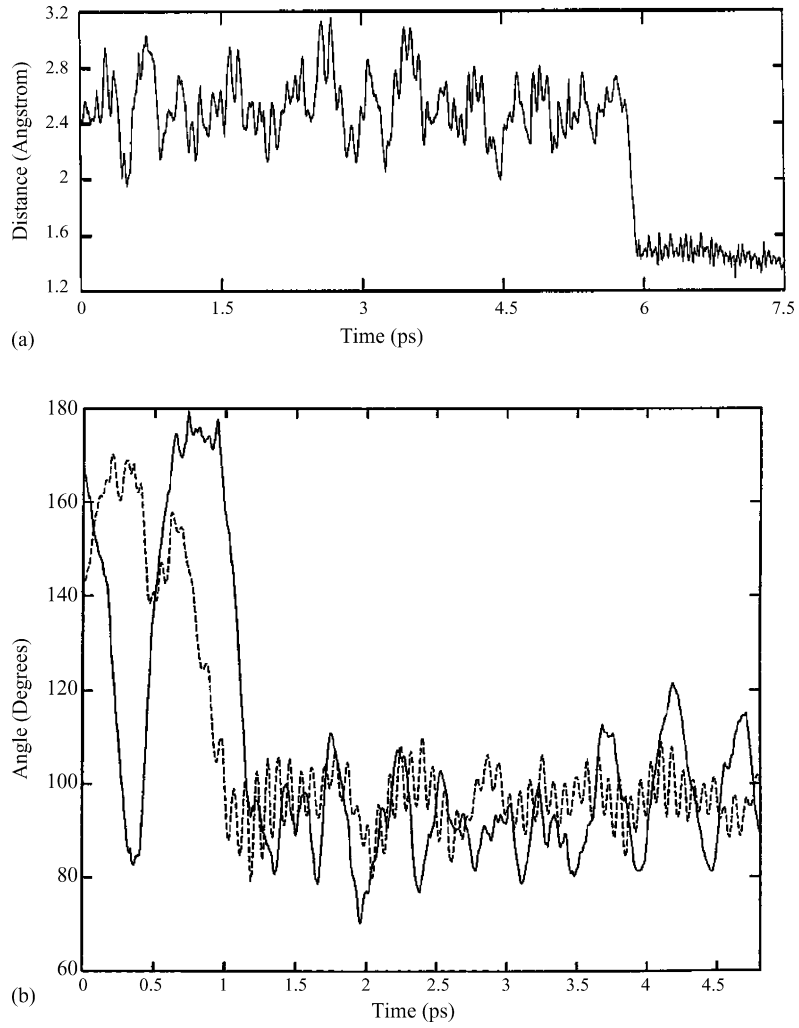

Fig. 7. (a) Time evolution of the C–C (carbonyl–vinyl) distance during the entire dynamics simulation. Time in ps and distances in Å. (b) Time evolution of the Cl–Ni–C (chlorine–vinyl) (solid line) and C–Ni–C angle (carbonyl–carbonyl) (dashed line) for the first part of the dynamics simulation. Time in ps and angles in degrees.

Two different mechanism have been proposed for the metal-assisted isomerization of 1-alkynes to vinylidenes (see Scheme 5). One is essentially the same mechanism occurring in the free acetylene–vinylidene tautomerization, with an approach of the metal to C_α and a concomitant 1,2-hydrogen shift from C_α to C_β (pathway 1A in Scheme 5). On the basis of photochemical studies on manganese and rhenium vinylidene complexes, Antonova and co-workers [41] proposed an alternative mechanism in which an oxidative addition of the 1-alkyne to the metal center gives a hydrido–alkynyl complex which then isomerizes by a 1,3-hydrogen shift from the metal to C_β (pathway 2 in Scheme 5). We review here the results of AIMD simulations and static DFT calculations performed on pathways 1A, 1B and 2 of Scheme 5, considering the prototypical $(Cp)(CO)_2Mn(HC{\equiv}CH)$ complex [7a]. In two subsequent studies we investigated the isomerization of 1-alkynes to vinylidenes on a series of cationic Ru(II) complexes [7b,7c]. We notice that Silvestre and Hoffmann [42] investigated the acetylene to vinylidene isomerization in the same $(Cp)(CO)_2Mn(HC{\equiv}CH)$ complex by means of semi-empirical calculations.

We started our analysis by searching equilibrium structures on the potential energy surface of the C_2H_2 unit bound to the $Cp(CO)_2Mn$ fragment. We have found altogether five minima, i.e. the acetylene complex **9**, the vinylidene complex **10**, an η^2-bound vinylidene complex **11**, an η^2-C–H coordinated acetylene complex **12** and a hydrido–alkynyl complex **13**. Structures and main geometrical parameters for complexes **9**–**13** can be found in Fig. 9. The vinylidene complex **10** is found as the global energy minimum structure and is 10.2 kcal/mol lower than the acetylene complex **9**. A careful inspection of pathway 1A (see below) has revealed the presence of an unusual η^2-bound vinylidene complex, **11**, which is 38.7 kcal/mol higher in energy than the more stable η^1-bound isomer **10**. A stable minimum corresponding to an η^2-C–H coordination of the acetylene moiety to the metal, **12**, was found 14.3 kcal/mol higher in energy than **9**. This η^2-C–H coordinated species is the natural precursor of the oxidative addition of the acetylene C−H bond to the metal center leading to a hydrido–alkynyl complex (pathway 2). The hydrido–alkynyl complex **13** was found 6.9 kcal/mol higher in energy than **12**.

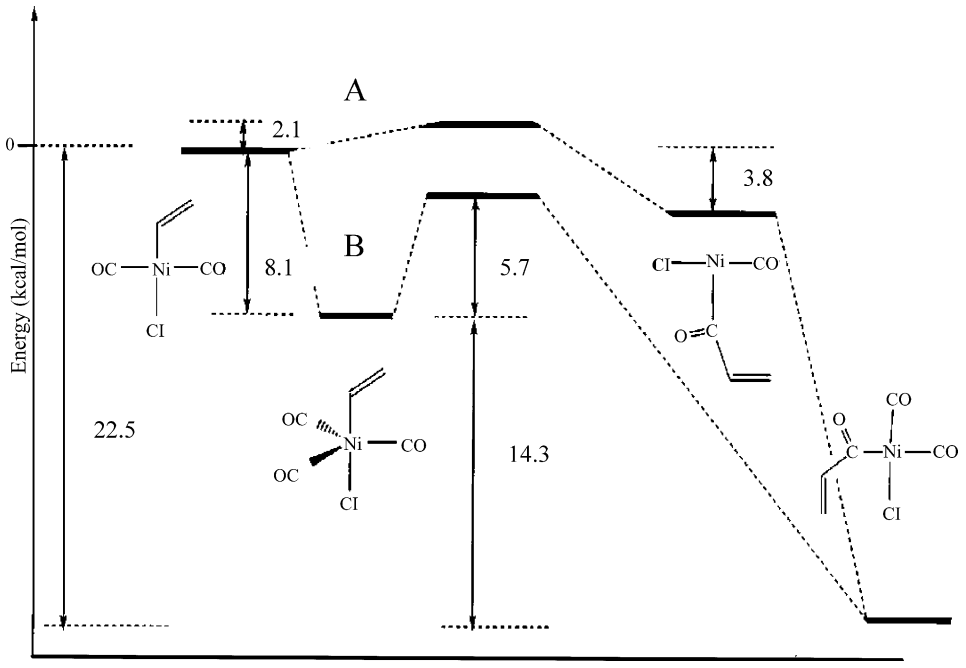

Fig. 8. Schematic representation of the potential energy surfaces for the two possible pathways A and B for CO insertion. Energies in kcal/mol.

5.1. Pathway 1A

In order to gain insight into the reaction mechanisms leading to the formation of the vinylidene complex **10** and to provide a guess for the transition state structures connecting the various minima on the reactive potential energy surface, we performed constrained AIMD simulations starting from complex **9**. We choose to constrain the C_β–H distance, expecting this parameter to connect the reagent and the product basins, by varying it from a value of 2.2 Å, corresponding to **9** to 1.1 Å, corresponding to **10**, as a function of the simulation time. The total time span of the simulation was 10 ps.

The evolution of the hydrogen shift can be followed by studying the time evolution of C_α–H and of the C_β–Mn distances. Indeed, the C_α–H distance is ca 1.1 Å in the reagent **9**, where the H atom is directly bound to the α carbon, while it grows up to ca. 2.2 Å in the product **10** where they are no longer bound. On the other hand, the C_β–Mn distance is ca. 2.1 Å in **9**, growing up to ca 3.1 Å in **10**, reflecting the detaching of the β carbon from the metal. To analyze the reaction mechanism in better detail,

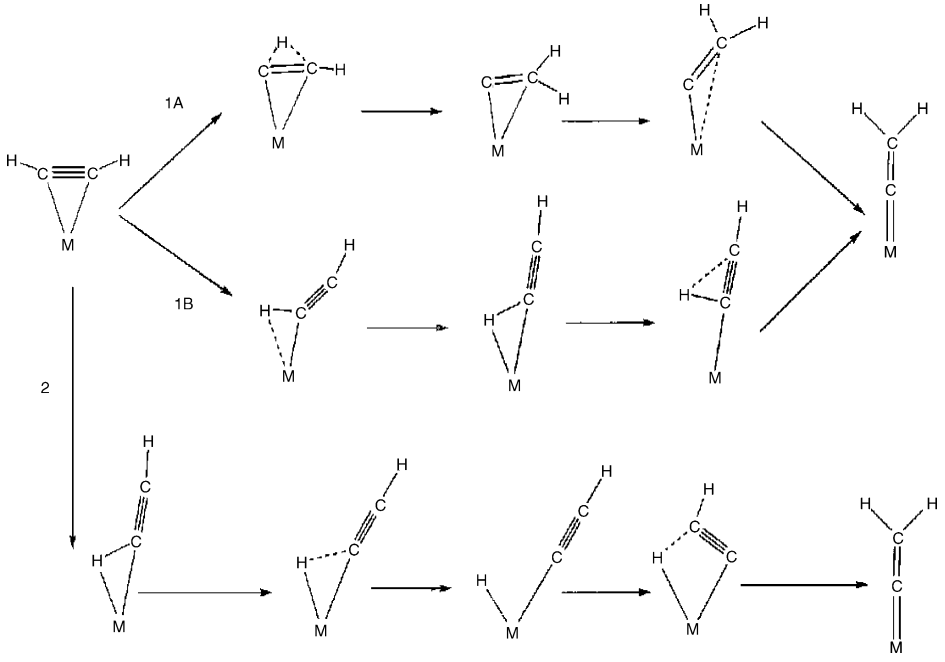

Scheme 5.

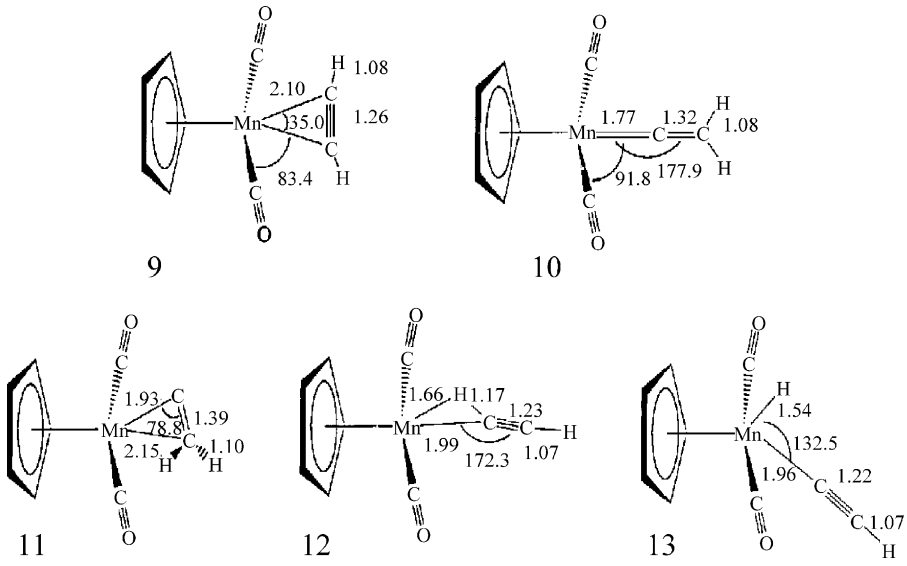

Fig. 9. Structures and main optimized geometrical parameters (Å, degree) for the acetylene **9**, vinylidene **10**, η^2-bound vinylidene **11**, η^2-C–H agostic acetylene **12** and alkynyl–hydrido **13** complexes.

Fig. 10a displays the variation of the considered parameters as a function of the C_β–H distance only in the range 1.30–1.15 Å, corresponding to the time span going from ca. 8 to ca. 9 ps. As it can be noticed, a 1,2-hydrogen shift takes place for a RC value close to 1.26 Å as suggested by the fast increase in the C_α–H distance observed between 1.26 and 1.24 Å; thereafter, this parameter keeps on oscillating around 2.2 Å, a value characteristic of the vinylidene complex **10**. It is interesting to notice how the C_β–Mn distance exhibits a similar behavior, even if its increase to ca. 3.1 Å, characteristic of complex **10**, is delayed of ca. 0.04 Å along the RC axis, corresponding to ca. 0.4 ps in time, suggesting that the 1,2-shift takes place prior to decoordination of the β carbon from the metal therefore indicating the presence of a transient η^2-bound vinylidene species, **11**. The short time stability of complex **11**, ca. 0.4 ps, suggests that a small energy barrier connects **11** to the more stable η^1-bound vinylidene **10**. Moreover, we did not observe the formation of the η^2-C−H acetylene species **12**, suggesting that a direct 1,2-shift is indeed a viable pathway to the formation of **10**.

Motivated by these results, we optimized the geometry of the η^2-bound vinylidene **11**, finding it to be a real minimum on the potential energy surface, 38.7 kcal/mol higher in energy than the η^1-bound isomer **10** and 28.5 kcal/mol above **9**. To the best of our knowledge an η^2-bound vinylidene species has never been detected, all structurally characterized vinylidene complexes assuming the usual η^1-coordination mode. By extracting selected configurations from the AIMD simulation we were also able to locate the transition state corresponding to the conversion between **9** and **11**, finding a structure 47.4 kcal/mol higher than **9**; the transition state corresponding to the conversion between **11** and **10** was found only 3.7 kcal/mol above **11**, in agreement with the short time stability of such a species observed during the dynamics simulations. A schematic representation of the potential energy surface for the overall direct 1,2-shift has been reported in Fig. 11a, from which it appears that formation of **11** is the rate determining step.

5.2. Pathway 1B

In order to rationalize the role played by complex **12** in the formation of **10**, we performed constrained AIMD simulations starting from **12**, constraining the C_β–H distance to vary from a value of 2.2 Å corresponding to **12**, to 1.1 Å, corresponding to **10**, as a function of the simulation time. The total time span of the simulation was again 10 ps. The evolution of the hydrogen shift can be followed by studying the time evolution of C_α–H and of the Mn–H distances. Indeed, the C_α–H distance is ca 1.2 Å in complex **12**, where the H atom is directly bound to the α carbon, while it grows up to ca. 2.1 Å in the product **10** where they are no longer bound. On the other hand, the Mn–H distance is ca. 1.7 Å in **12**, growing up to ca. 3.8 Å in **10** as a consequence of the hydrogen shift to the β carbon. Fig. 10b displays the variation of the considered parameters as a function of the C_β–H distance for the entire range of variation of this parameter. As it can be noticed, the hydrogen shift takes place for a C_β–H distance close to 1.42 Å as suggested by the fast increase in the C_α–H distance observed between 1.42 and 1.40 Å. From Fig. 10b, we can notice that the hydrogen detachment from the metal takes place prior to hydrogen migration, suggesting a transition state in which the decoordinated H atom is still exploiting the bonding interaction with the α carbon. Inspection of the time evolution of the $\angle HC_\alpha Mn$ and of the $\angle MnC_\alpha C_\beta$ angles (not shown) revealed that the H decoordination from the metal takes place prior to migration, and that the 1,2-shift does not affect the $\angle MnC_\alpha C_\beta$ angle, which remains approximately linear along the whole time evolution. This suggests that the transition state structure is stabilized by the partial formation of the incoming double metal–carbon bond which makes stiffer the $\angle MnC_\alpha C_\beta$ angle.

By extracting selected configurations from the AIMD simulation we optimized the transition state corresponding to the conversion between **12** and **10**, finding a structure 16.1 kcal/mol higher than **12** and therefore 30.4 kcal/mol higher than **9**. More-

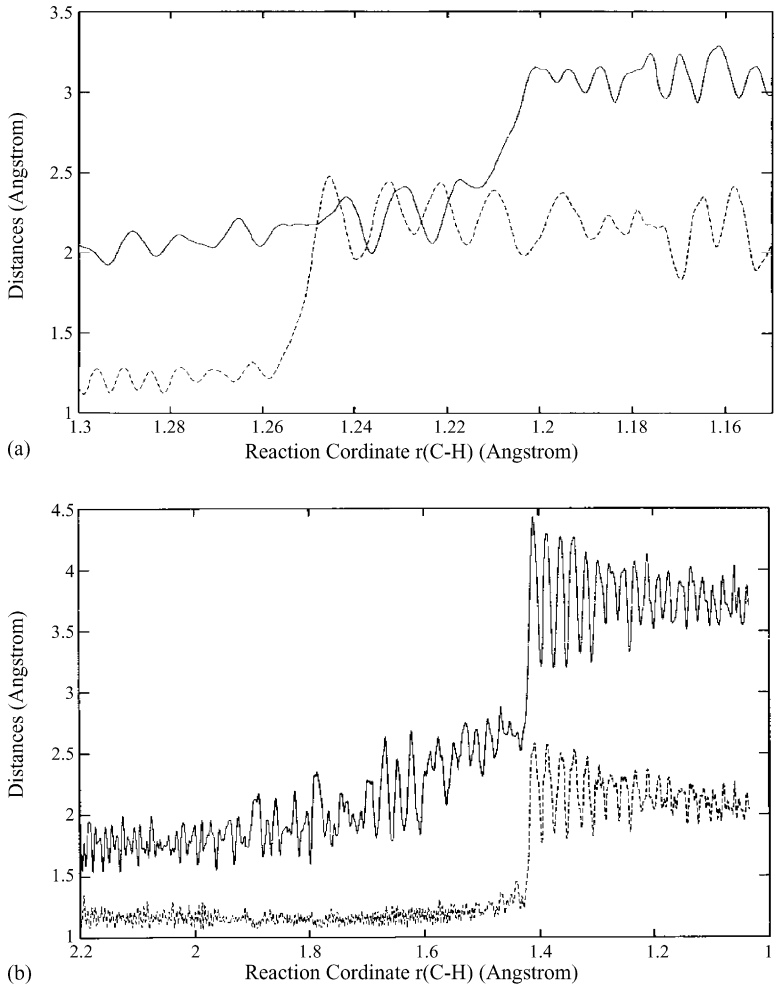

Fig. 10. (a) Time evolution of the C_α–H (dashed line) and C_β–Mn (solid line) distances (Å) for the dynamics simulation starting from the acetylene complex **1** in the RC range 1.30–1.15 Å (8–9 ps). (b) Time evolution of the Mn–H (solid line) and C_α–H (dashed line) distances (Å) for the dynamics simulation starting from the η^2-C–H agostic acetylene complex **12** in the RC range 2.20–1.10 Å (0–10 ps).

over, we were able to locate the transition state structure corresponding to the slippage process from **9** to **12**, finding it 27.5 kcal/mol higher than **9**. A schematic representation of the potential energy surface for the overall hydrogen shift in pathway 1B has been reported in Fig. 11b; as it can be noticed the highest barrier to the formation of **10** is computed to be only 30.4 kcal/mol, i.e. 17.0 kcal/mol lower than the value computed for the direct 1,2-shift of pathway 1A.

5.3. Pathway 2

We localized the transition state for the oxidative addition leading from the agostic intermediate **12** to the hydrido–alkynyl complex **13**, finding a structure 24.4 kcal/mol higher than **12**, therefore 38.7 kcal/mol above the acetylene complex **9**. The computed energy barrier is 8.3 kcal/mol higher than that for the 1,2-shift from the agostic intermediate **12**, so that the intermediacy of **13** in the formation of **10** seems unlikely.

We finally localized the transition state corresponding to the 1,3- hydrogen shift leading from **13** to **11**, finding a structure 25.1 kcal/mol above **13**, therefore 46.3 kcal/mol above **9**. A schematic representation of the potential energy surface for the intramolecular 1,3-hydrogen shift in pathway 2 has been reported in Fig. 11c. These results suggest that an eventual hydrido–alkynyl to vinylidene rearrangement would probably follow an intermolecular rather than an intramolecular pathway, as found by Morokuma and co-workers for the $[Cl(PH_3)_2Rh(HC{\equiv}CH)]$ system [43a].

Since a pseudo-octahedral hydrido–alkynyl d^4 species would be expected to have a triplet ground state, we checked whether higher spin configurations play a role in determining the energetics of pathway 2, and optimized the geometry of the hydrido–alkynyl complex **13** considering also triplet and quintet spin-multiplicities. As expected, the singlet spin state turned out to be ground state, with the triplet and quintet states 36.6 and 58.9 kcal/mol higher in energy. For the sake of completeness, we also re-optimized the transition state for the conversion from **12** to **13** imposing a triplet spin-multiplicity, finding a structure 20.6 kcal/mol above the singlet optimized transition state structure. The participation of higher spin energy surfaces can be therefore ruled out for the investigated process.

The situation is considerably different for cationic Ru(II) complexes, for which we found a considerable stabilization of the hydrido–alkynyl intermediate upon increasing the electron

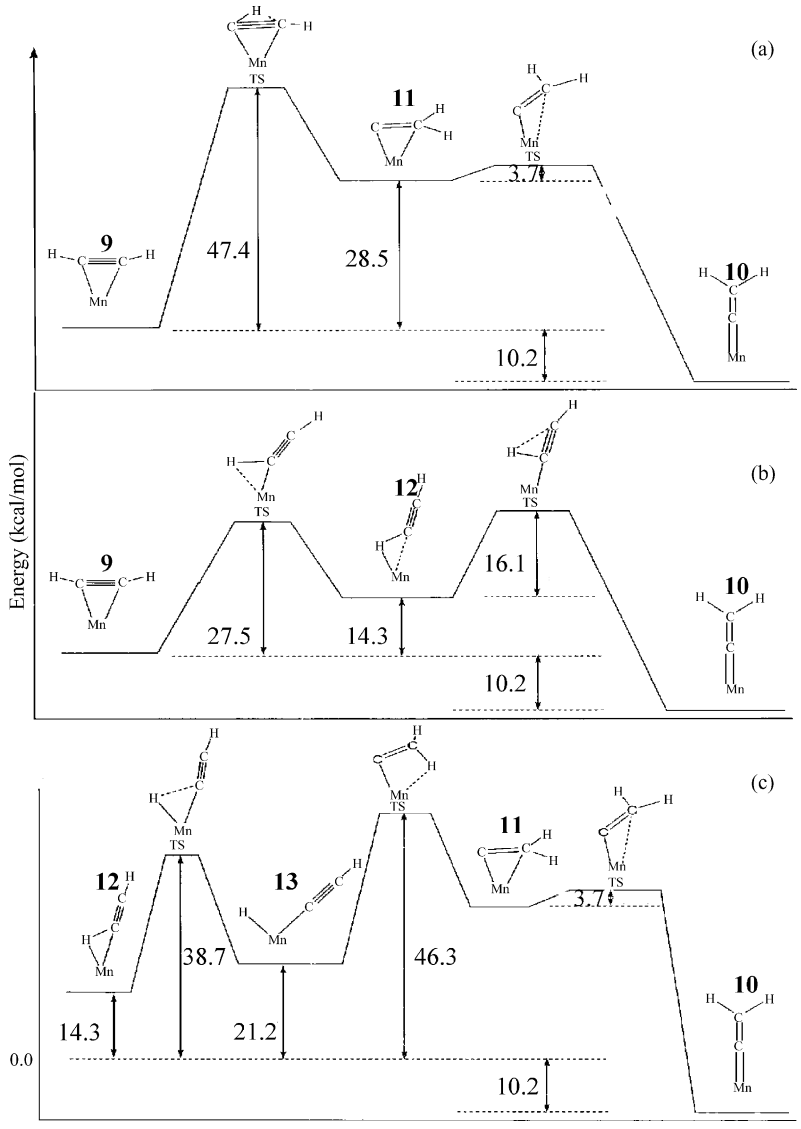

Fig. 11. (a–c) Schematic representation of the potential energy surface for the 1,2-hydrogen shifts of pathways 1A, 1B and 2. Energies in kcal/mol.

richness of the metal center [7b,7c], as opposed to the situation found for the electron poor $[Cl_2Ru(PH_3)_2(HC{\equiv}CH)]^+$ complex [43b]. In particular, a linear correlation has been found between the C=C stretching frequencies of the vinylidene complexes, as an estimate of the electron richness, and the stability of the corresponding hydrido–alkynyl intermediates for a series of different metal fragments of increasing electron richness [7c]. It is worth mentioning that for the most electron-rich $[(Cp^*)(dippe)Ru(HCCH)]^+$ species among the considered Ru(II) complexes, the hydrido–alkynyl species has been calculated to be essentially isoenergetic with the alkyne complex (only 1.9 kcal/mol higher), in agreement with the experimental evidence showing in this system an equilibrium between these two species [44a] and with theoretical results for a similar complex [44b]. For the same $[(Cp^*)(dippe)Ru]^+$ fragment, a detailed analysis of the reaction profiles for the two possible acetylene rearrangement pathways 1 and 2, has shown that once the η^2-C–H coordinated acetylene intermediate is accessed, the system can easily evolve toward a hydrido–alkynyl species, this process being kinetically favored with respect to the direct 1,2-shift leading to the vinylidene product. The hydrido–alkynyl species may then evolve to the final vinylidene product, through either a reverse reductive elimination to the η^2-C–H coordinated acetylene intermediate, which then undergoes a 1,2-hydrogen shift as in pathway 1B or most likely an intermolecular 1,3-hydrogen shift [43a] or a deprotonation/reprotonation mechanism [44a]. An intramolecular 1,3-shift seems quite unlikely since for the similar $[(Cp)(PMe_3)_2Ru]^+$ fragment we calculated an energy barrier as high as 51.1 kcal/mol for this process [7b].

6. Oxidative addition of SiH_4 to $Pt(PH_3)_2$

Oxidative addition of the Si–H bond to transition metal complexes is involved as a key step in the metal-catalyzed hydrosilylation of a wide variety of substituted alkenes, dienes and alkynes, leading to many different organosilicon compounds. One of the best known catalysts for hydrosilylation is chloroplatinic acid (Speier's catalysts) [45], for which Chalk and Harrod

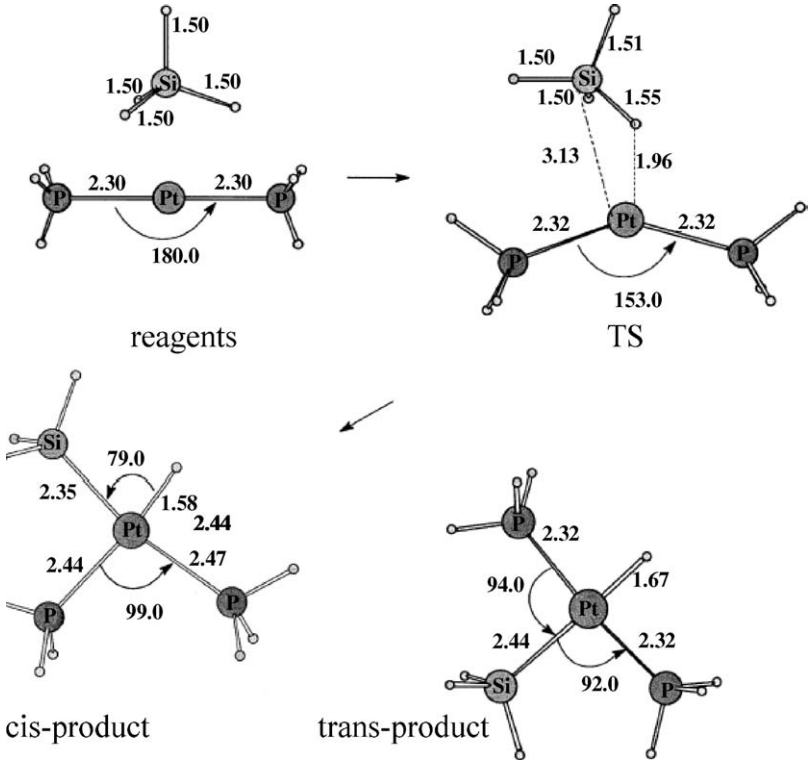

Fig. 12. Structures and main optimized geometrical parameters (Å, degree) for the reagents, transition state and products of the oxidative addition of SiH_4 to $Pt(PH_3)_2$.

[46] have proposed a reaction mechanism consisting of Si–H oxidative addition to the metal, alkene insertion into Pt–H bond and Si–C reductive elimination to give the final organosilicon compound (see Scheme 6).

Although the active species of Speier's catalyst is still ambiguous, experimental investigations suggested that the preliminary Si–H oxidative addition of this hydrosilylation reaction occurs to a Pt(0) diphosphine complex [47].

We review here the results of AIMD simulations and static DFT calculations on the reaction between SiH_4 and $Pt(PH_3)_2$, focusing our attention on the Si–H oxidative addition to $Pt(PH_3)_2$

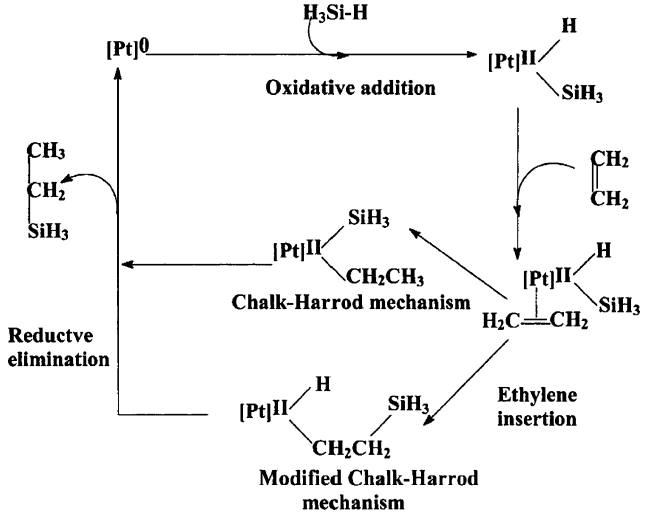

Scheme 6.

[8a]. The characterization of the entire catalytic cycle was reported by Sakaki et al. [48] and by us [8b–8d].

To gain insight into the reaction mechanism of the oxidative addition step, we performed AIMD simulations starting from the SiH_4 and $Pt(PH_3)_2$ reagents. Previous calculations [48] on the Si–H oxidative addition to $Pt(PH_3)_2$ revealed a small energy barrier and a quite large exothermicity for this process. Constrained AIMD simulations were performed by varying the Si–Pt distance in the range 4.6–2.3 Å, the former value corresponding to the unbound free reagents, the latter being close to the Si–Pt bond distance in the product of the oxidative addition, a $PtH(PH_3)_2$–SiH_3 square-planar complex (see Fig. 12). Even though other approximate reaction coordinates might be conceived, the Si–Pt distance should represent a reasonable choice since its decrease corresponds to a shortening of the distance between the SiH_4 and $Pt(PH_3)_2$ fragments, without explicitly involving variations of geometrical parameters connected to the migrating H-atom, which, therefore, can freely adopt the more convenient geometrical arrangement. AIMD simulations were initialized by fixing the Si–Pt distance at 4.6 Å, optimizing the corresponding structure, and thermalising the resulting system at 300 K for 1.4 ps; subsequently, we constrained the Si–Pt distance to decrease to 2.3 Å during a time span of 5.8 ps.

The oxidative addition reaction can be followed by studying the time evolution of the Pt–H and Si–H distances, which are, respectively, supposed to decrease and increase from their initial values in the isolated reagents, testifying, respectively, the H atom migration to Pt and the breaking of the Si–H bond. These two parameters have been reported in Fig. 13a as a function of the simulation time (approximate reaction coordinate); as it can

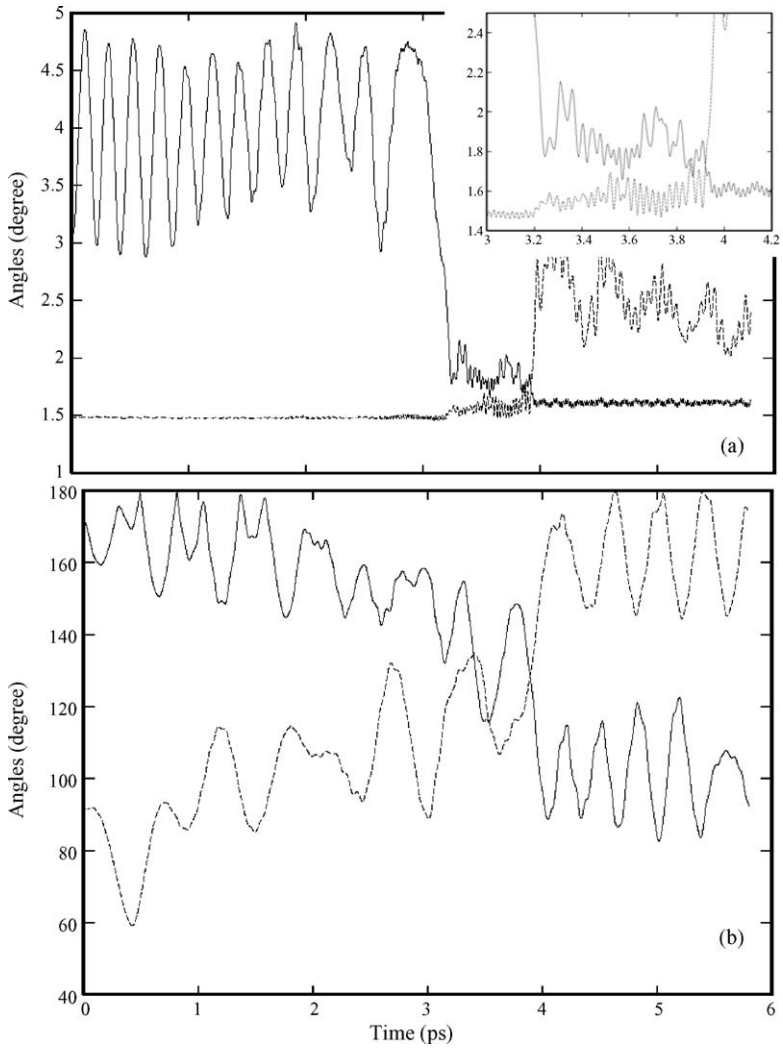

Fig. 13. (a) Time evolution of the Pt–H (solid line) and Si–H (dashed line) distances for the entire time span of the simulation (0–6 ps). *Inset*: time evolution of the Pt–H (solid line) and Si–H (dashed line) distances for the 3–4.2 ps time span. Time in ps and distances in Å. (b) Time evolution of the ∠P–Pt–P (solid line) and ∠Si–Pt–P (dashed line) angles for the entire time span of the simulation (0–6 ps). Time in ps and angles in degree.

be noticed, the oxidative addition reaction begins after 3.0 ps and is completed within 4.0 ps, as shown by the fast decrease of the Pt–H distance from ca. 4.7 Å, corresponding to the free unbound reagents, to 1.6 Å, close to its equilibrium value in the final product in which the H atom has migrated to the coordination sphere of the Pt atom. The Si–H distance follows an almost complementary trajectory with respect to the Pt–H distance, increasing from ca. 1.5 to 3.0 Å after 4.0 ps, reflecting H atom detachment from the SiH_3 group following H migration. It is interesting to analyse the variation of the Pt–H and Si–H distances in more detail for the time span corresponding to the reactive event (3.0–4.0 ps). The results are presented in the inset of Fig. 13a and show that formation of the incipient Pt–H bond takes place before breaking of the Si–H bond is observed, as results from the delay of ca. 0.8 ps occurring between Pt–H distance decrease (ca. 3.2 ps) and Si–H detachment (ca. 4.0 ps). The resulting geometrical arrangement shows a trigonal coordination with a forming Pt–H bond (ca. 1.8 Å) and still a short Si–H distance (ca. 1.5 Å), with a Si–Pt distance close to 2.8 Å, suggesting a transition state structure characterized by the simultaneous interaction of the migrating H atom both with the Si and Pt centers.

Further insight into the reaction mechanism can be gained by analysing the variation of the ∠P–Pt–P and of the ∠Si–Pt–P angles, reported as a function of the simulation time in Fig. 13b. The ∠P–Pt–P angle characterizes the relative *cis-trans* arrangement of the two phosphine ligands, while the ∠Si–Pt–P angle characterizes the relative orientation of the SiH_4 and $Pt(PH_3)_2$ groups. From Fig. 13b, it appears that the oxidative addition leads directly to the *cis* square-planar product, as testified by the oscillations of the ∠P–Pt–P angle around 100° after 4.0 ps; variation of the considered parameter from ca. 180° to 100 ° reflects the change in the Pt coordination from a linear to square-planar environment. Moreover, evolution of the ∠Si–Pt–P angle shows that the SiH_4 attack to Pt takes place along a line bisecting the ∠P–Pt–P angle, on the bent $Pt(PH_3)_2$ fragment as shown by the oscillations of the considered parameter around 120° between 3.0 and 4.0 ps, in correspondence to H migration.

Extracting selected configuration from the AIMD simulation, we optimized the transition state for the oxidative addition step,

finding a structure only 1.1 kcal/mol above the energy of the free reagents. In the transition state structure, the Si–H bond approaches the metal in an out-of-plane fashion with a dihedral angle between the Pt–Si–H and P–Pt–P planes of about 52°, see Fig. 12. Geometry optimizations of both the *cis* and *trans* isomers of the $Pt(PH_3)(H)(SiH_3)$ reaction product have shown that the *cis* isomer is more stable by 11.7 kcal/mol than the *trans* isomer, consistent with the results of AIMD simulations showing the direct formation of the more stable *cis*-$Pt(PH_3)(H)(SiH_3)$ product. Overall, the oxidative addition is exothermic by 22.2 kcal/mol, suggesting that this process is both kinetically and thermodynamically favored.

7. Concluding remarks

We have presented an overview of our activity in the field of ab initio molecular dynamics simulations of organometallic reactivity. In particular, we have provided examples of how Car–Parrinello molecular dynamics simulations allow us to dynamically sample the potential energy surface of the reactive system at finite temperature, providing useful insights into the reaction mechanism and evidencing the presence of reaction intermediates. Ultimately, by combining dynamics simulations with static DFT calculations of the stationary points of the reactive potential energy surface, the energetics and reaction mechanism of complex organometallic reactions have been explored. This combined computational strategy has been applied to a wide range of prototypical organometallic reactions, including migratory insertions of carbon monoxide and methylisocyanide into different metal–carbon bonds, the SiH oxidative addition to $Pt(PH_3)_2$ and the acetylene to vinylidene isomerization in the coordination sphere of a transition metal center.

Acknowledgements

We thank Prof. N. Re for helpful and stimulating discussions and Dr. G. Giorgi for static DFT calculations on the SiH_4 oxidative addition to $Pt(PH_3)_2$.

References

[1] R. Car, M. Parrinello, Phys. Rev. Lett. 55 (1985) 2471.
[2] R. Car, F. De Angelis, P. Giannozzi, N. Marzari, in: S. Yip (Ed.), Handbook of Materials Modeling, vol. XXXIX, Hardcover Springer, 2005, p. 2965.
[3] (a) P. Margl, T. Ziegler, P.E. Blöchl, J. Am. Chem. Soc. 17 (1995) 12625;
(b) P. Margl, J.C.W. Lohrenz, T. Ziegler, P. E. Blöchl, J. Am. Chem. Soc. 118 (1996) 4434;
(c) P. Margl, T. Ziegler, P.E. Blöchl, J. Am. Chem. Soc. 118 (1996) 5412;
(d) T.K. Woo, P.M. Margl, J.C.W. Lohrenz, P.E. Blöchl, T. Ziegler, J. Am. Chem. Soc. 118 (1996) 13021;
(e) T.K. Woo, P.M. Margl, P.E. Blöchl, T. Ziegler, J. Phys. Chem. B 101 (1997) 7877;
(f) T.K. Woo, P.M. Margl, T. Ziegler, P.E. Blöchl, Organometallics 16 (1997) 3454;
(g) P.M. Margl, T.K. Woo, P.E. Blöchl, T. Ziegler, J. Am. Chem. Soc. 120 (1998) 2174;
(h) T.K. Woo, P.E. Blöchl, T. Ziegler, J. Phys. Chem. A 104 (2000) 121;
(i) A. Michalak, T. Ziegler, J. Phys. Chem. A 105 (2001) 4333;
(l) M. Cheong, M. Schmid, T. Ziegler, Organometallics 19 (2000) 1973;
(m) M.S.W. Chan, T. Ziegler, Organometallics 19 (2000) 5182;
(n) A. Michalak, T. Ziegler, Organometallics 22 (2003) 2660;
(o) M.J. Szabo, N.M. Galea, A. Michalak, S.-Y. Yang, L.F. Groux, W.E. Piers, T. Ziegler, Organometallics 24 (2005) 2147;
(p) R.L. DeKock, I.H. Hristov, J.D.W. Anderson, I. Göttker-Schnetmann, S. Mecking, T. Ziegler, Organometallics 24 (2005) 2679;
(q) T. Ziegler, J. Autschbach, Chem. Rev. 105 (2005) 2695.
[4] (a) F. De Angelis, A. Sgamellotti, N. Re, Organometallics 19 (2000) 4904;
(b) F. De Angelis, A. Sgamellotti, N. Re, Organometallics 19 (2000) 4104;
(c) F. De Angelis, A. Sgamellotti, N. Re, J. Chem. Soc., Dalton. Trans. (2001) 1023.
[5] (a) S. Fantacci, F. De Angelis, A. Sgamellotti, N. Re, Organometallics 20 (2000) 4031;
(b) S. Fantacci, F. De Angelis, A. Sgamellotti, N. Re, Organometallics 21 (2002) 4090;
(c) F. De Angelis, S. Fantacci, A. Sgamellotti, N. Re, Theor. Chem. Acc. 110 (2003) 196;
(d) F. De Angelis, A. Sgamellotti, N. Re, S. Fantacci, Organometallics 24 (2005) 1867.
[6] (a) F. De Angelis, N. Re, A. Sgamellotti, A. Selloni, J. Weber, C. Floriani, Chem. Phys. Lett. 291 (1998) 57;
(b) F. De Angelis, A. Sgamellotti, N. Re, Organometallics 19 (2000) 4104;
(c) F. De Angelis, A. Sgamellotti, N. Re, Organometallics 21 (2002) 2036.
[7] (a) F. De Angelis, A. Sgamellotti, N. Re, Organometallics 21 (2002) 2715;
(b) F. De Angelis, A. Sgamellotti, N. Re, Organometallics 21 (2002) 5944;
(c) F. De Angelis, A. Sgamellotti, N. Re, Dalton Trans. 20 (2004) 3225.
[8] (a) G. Giorgi, F. De Angelis, N. Re, A. Sgamellotti, Chem. Phys. Lett. 364 (2002) 87;
(b) G. Giorgi, F. De Angelis, N. Re, A. Sgamellotti, J. Mol. Struct. Theochem 623 (2003) 277;
(c) G. Giorgi, F. De Angelis, N. Re, A. Sgamellotti, Computational Science-ICCS, PT II, Proceedings Lecture Notes in Computer Science, vol. 2658, 2003, p. 331;
(d) G. Giorgi, F. De Angelis, N. Re, A. Sgamellotti, Fut. Gen. Comp. Syst. 20 (2004) 781.
[9] F. Nunzi, F. Mercuri, F. De Angelis, A. Sgamellotti, N. Re, P. Giannozzi, J. Phys. Chem. B 108 (2004) 5243.
[10] (a) M. Boero, M. Parrinello, K. Terakura, J. Am. Chem. Soc. 120 (1998) 2746;
(b) O.M. Aagaard, R.J. Meier, F. Buda, J. Am. Chem. Soc. 120 (1998) 7174;
(c) B.B. Coussens, F. Buda, H. Oevering, R.J. Meier, Organometallics 17 (1998) 795;
(d) U. Burckhardt, G.L. Casty, D. Tilley, T.K. Woo, U. Rothlisberger, Organometallics 19 (2000) 3830;
(e) M. Boero, M. Parrinello, S. Hüffer, K. Terakura, J. Am. Chem. Soc. 122 (2000) 501;
(f) H.M. Senn, P.E. Blöchl, A. Togni, J. Am. Chem. Soc. 122 (2000) 4098;
(g) A. Magistrato, J. VandeVondele, U. Rothlisberger, Inorg. Chem. 39 (2000) 5553;
(h) A.J. Sillanpää, K.E. Laasonen, Organometallics 20 (2001) 1334;
(i) A. Magistrato, T.K. Woo, A. Togni, U. Rothlisberger, Organometallics 23 (2004) 3218;
(j) B. Ensing, F. Buda, M.C.M. Gribnau, E.J. Baerends, J. Am. Chem. Soc. 126 (2004) 4355;
(k) A. Stirling, M. Iannuzzi, M. Parrinello, F. Molnar, V. Bernhart, G.A. Luinstra, Organometallics 24 (2005) 2533;
(l) M. Bühl, S. Grigoleit, Organometallics 24 (2005) 1516.
[11] D. Vanderbilt, Phys. Rev. B 41 (1990) 7892.
[12] (a) F. De Angelis, Ph.D. Thesis, University of Perugia, 1999;
(b) P. Giannozzi, F. De Angelis, R. Car, J. Chem. Phys. 120 (2004) 5903.
[13] (a) A. Pasquarello, K. Laasonen, R. Car, C. Lee, D. Vanderbilt, Phys. Rev. Lett. 69 (1992) 1982;
(b) A. Pasquarello, K. Laasonen, R. Car, C. Lee, D. Vanderbilt, Phys. Rev. B 47 (1993) 10142.
[14] J.P. Perdew, A. Zunger, Phys. Rev. B 23 (1981) 5048.
[15] J.P. Perdew, J.A. Chevary, S.H. Vosko, K.A. Jackson, M.R. Pederson, D.J. Singh, C. Fiolhais, Phys. Rev. B 46 (1992) 6671.

[16] J.-P. Ryckaert, G. Ciccotti, H.J. Berendsen, J. Comp. Phys. 23 (1977) 327.
[17] T.P. Straatsma, H.J.C. Berendsen, J.P.M. Postma, J. Chem. Phys. 85 (1986) 6720.
[18] S. Nosé, Mol. Phys. 52 (1984) 255;
W.G. Hoover, Phys. Rev. A 31 (1985) 1695.
[19] (a) E.J. Baerends, D.E. Ellis, P. Ros, Chem. Phys. 2 (1973) 42;
(b) E.G. te Velde, E.J. Baerends, J. Comp. Phys. 99 (1992) 84;
(c) C. Fonseca Guerra, O. Visser, J.G. Snijders, G. te Velde, E.J. Baerends, in: E. Clementi, G. Corongiu (Eds.), Methods and Techniques for Computational Chemistry, STEF, Cagliari, 1995, p. 305;
(d) E.G. te Velde, F.M. Bickelhaupt, E.J. Baerends, S.J.A. van Gisbergen, C. Fonseca Guerra, J.G. Snijders, T. Ziegler, J. Comput. Chem. 22 (2001) 931.
[20] M.J. Frisch, G.W. Trucks, H.B. Schlegel, G.E. Scuseria, M.A. Robb, J.R. Cheeseman, J.A. Montgomery, Jr., T. Vreven, K.N. Kudin, J.C. Burant, J.M. Millam, S.S. Iyengar, J. Tomasi, V. Barone, B. Mennucci, M. Cossi, G. Scalmani, N. Rega, G.A. Petersson, H. Nakatsuji, M. Hada, M. Ehara, K. Toyota, R. Fukuda, J. Hasegawa, M. Ishida, T. Nakajima, Y. Honda, O. Kitao, H. Nakai, M. Klene, X. Li, J.E. Knox, H.P. Hratchian, J.B. Cross, C. Adamo, J. Jaramillo, R. Gomperts, R.E. Stratmann, O. Yazyev, A.J. Austin, R. Cammi, C. Pomelli, J.W. Ochterski, P.Y. Ayala, K. Morokuma, G.A. Voth, P. Salvador, J.J. Dannenberg, V.G. Zakrzewski, S. Dapprich, A.D. Daniels, M.C. Strain, O. Farkas, D.K. Malick, A.D. Rabuck, K. Raghavachari, J.B. Foresman, J.V. Ortiz, Q. Cui, A.G. Baboul, S. Clifford, J. Cioslowski, B.B. Stefanov, G. Liu, A. Liashenko, P. Piskorz, I. Komaromi, R.L. Martin, D.J. Fox, T. Keith, M.A. Al-Laham, C.Y. Peng, A. Nanayakkara, M. Challacombe, P.M.W. Gill, B. Johnson, W. Chen, M.W. Wong, C. Gonzalez, J.A. Pople, Gaussian 03, Revision A.1, Gaussian Inc., Pittsburgh, PA, 2003.
[21] (a) M.J. Frisch, J.A. Pople, J.S. Binkley, J. Chem. Phys. 80 (2004) 3265, and references therein;
(b) P.J. Hay, J. Chem. Phys. 77 (1977) 4377;
(c) A.J.H. Wachters, J. Chem. Phys. 52 (1970) 1033.
[22] (a) P.J. Hay, W.R. Wadt, J. Chem. Phys. 82 (1985) 270;
(b) P.J. Hay, W.R. Wadt, J. Chem. Phys. 82 (1985) 284;
(c) P.J. Hay, W.R. Wadt, J. Chem. Phys. 82 (1985) 299.
[23] R. Ditchfield, W.J. Herhe, J.A. Pople, J. Comp. Chem. 54 (1971) 724.
[24] S.H. Vosko, L. Wilk, M. Nusair, Can. J. Phys. 58 (1980) 1200.
[25] (a) A.D. Becke, Phys. Rev. A 38 (1988) 3098;
(b) J.P. Perdew, Y. Wang, Phys. Rev. B 45 (1992) 13244.
[26] (a) E.J. Kulhmann, J.J. Alexander, Coord. Chem. Rev. 33 (1980) 195;
(b) A. Wojcicki, Adv. Organomet. Chem. 11 (1973) 97;
(c) T.C. Foold, in: G.L. Geoffry (Ed.), Topics in Stereochemistry, vol. 12, Wiley, New York, 1981, p. 83;
(d) J.J. Alexander, in: F.R. Hartley (Ed.), The Chemistry of the Metal–Carbon Bond, vol. 2, Wiley, New York, 1985;
(e) P.L. Bock, D.J. Boschetto, J.R. Rasmussen, J.P. Demeres, G.M. Whitesides, J. Am. Chem. Soc. 96 (1974) 2814;
(f) M.J. Wax, R.G. Bergman, J. Am. Chem. Soc. 103 (1981) 7028.
[27] (a) J.W. Lauher, R. Hoffmann, J. Am. Chem. Soc. 98 (1976) 1729;
(b) K. Tatsumi, A. Nakamura, P. Hofmann, P. Stauffert, R. Hoffmann, J. Am. Chem. Soc. 107 (1985) 4440;
(c) P. Hofmann, P. Stauffert, K. Tatsumi, A. Nakamura, R. Hoffmann, Organometallics 4 (1985) 404.
[28] (a) L.D. Durfee, I.P. Rothwell, Chem. Rev. 88 (1988) 1059;
(b) L.D. Durfee, A.K. McMuullen, I.P. Rothwell, J. Am. Chem. Soc. 110 (1988) 1463;
(c) R.L. Chamberlain, L.D. Durfee, P.E. Fanwick, R. Kobriger, S.L. Latesky, A.K. McMullen, I.P. Rothwell, K. Folting, J.C. Huffman, W.E. Streib, R. Wang, J. Am. Chem. Soc. 109 (1987) 390.
[29] L. Giannini, A. Caselli, E. Solari, C. Floriani, A. Chiesi-Villa, C. Rizzoli, N. Re, A. Sgamellotti, J. Am. Chem. Soc. 119 (1997) 9709.
[30] (a) G. Erker, F. Rosenfeldt, J. Organomet. Chem. 224 (1982) 29;
(b) G. Erker, Acc. Chem. Res. 17 (1984) 103.
[31] (a) M.J. Scott, S.J. Lippard, Organometallics 16 (1997) 5857;
(b) F.J. Berg, J.L. Petersen, Organometallics 10 (1991) 1599;(c) T.-G. Ong, D. Wood, G.P.A. Yap, D.S. Richeson, Organometallics 21 (2002) 1;
(d) A.M. Martins, J.R. Ascenso, C.G. de Azevedo, A.R. Dias, M.T. Duarte, J.F. da Silva, L.F. Veiros, S.S. Rodrigues, Organometallics 22 (2003) 4218.
[32] J.H. Hardesty, T.A. Albright, S. Kahlal, Organometallics 19 (2000) 4159.
[33] P. Powell, Principles of Organometallic Chemistry, Chapman & Nall, London, 1988.
[34] B. Cornils, W.A. Herrmann, Applied Homogeneous Catalysis with Organometallic Compounds, VCH, Weinheim, 1996.
[35] E. Drent, M. Catharina, T. De Kock, U.S. Patent 5,688,909 (1997).
[36] (a) C.S. Shultz, J.M. DeSimone, M. Brookhart, Organometallics 20 (2001) 16;
(b) C.S. Shultz, J.M. DeSimone, M. Brookhart, J. Am. Chem. Soc. 123 (2001) 9172.
[37] (a) J.P. Collman, L.S. Hegedus, J.R. Norton, R.G. Finke, Principles and Applications of Organotransition Metal Chemistry, University Science Books, Mill Valley, CA, 1987;
(b) H.M. Colquhoun, D.J. Thompson, M.V. Twigg, Carbonylation, Direct Synthesis of Carbonyl Compounds, Plenum Press, New York, 1991;
(c) G.W. Parshall, S.D. Ittel, Homogeneous Catalysis, second ed., Wiley, New York, 1992.
[38] (a) F.A. Cotton, G. Wilkinson, Advanced Inorganic Chemistry, fifth ed., Wiley/Interscience, New York, 1988;
(b) M.I. Bruce, Chem. Rev. 98 (1998) 2797;
(c) F. Zaera, Chem. Rev. 95 (1995) 2651.
[39] (a) Y. Chen, D.M. Jonas, C.E. Hamilton, P.G. Green, J.L. Kinsey, R.W. Field, Ber. Bunsen-Ges. Phys. Chem. 92 (1998) 329;
(b) Y. Chen, D.M. Jonas, J.L. Kinsey, R.W. Field, J. Chem. Phys. 91 (1989) 3976;
(c) K.M. Erwin, J. Ho, W.C. Lineberger, J. Chem. Phys. 91 (1989) 5974;
(d) K.M. Erwin, S. Gronert, S.E. Barlow, M.K. Gilles, A.G. Harrison, V.M. Bierbaum, C.H. DePuy, W.C. Lineberger, G.B. Ellison, J. Am. Chem. Soc. 112 (1990) 5750.
[40] (a) H. Werner, Angew. Chem. Int. Ed. Engl. 29 (1990) 1077;
(b) M.I. Bruce, Chem. Rev. 91 (1991) 197.
[41] (a) A.N. Nesmeyanov, G.G. Alexandrov, A.B. Antonova, K.N. Anisimov, N.E. Kolobova, Yu.T. Struchkov, J. Organomet. Chem. 110 (1976) 36;
(b) A.B. Antonova, N.E. Kolobova, P.V. Petrovsky, B.V. Lokshin, N.S. Obezyuk, J. Organomet. Chem. 137 (1977) 55.
[42] J. Silvestre, R. Hoffmann, Helv. Chim. Acta 68 (1985) 1461.
[43] (a) Y. Wakatsuki, N. Koga, H. Werner, K. Morokuma, J. Am. Chem. Soc. 119 (1977) 360;
(b) Y. Wakatsuki, N. Koga, H. Yamazaki, K. Morokuma, J. Am. Chem. Soc. 116 (1994) 8105.
[44] (a) I. de Los Rios, M. Jimenez-Tenorio, M.C. Puerta, P. Valerga, J. Am. Chem. Soc. 119 (1997) 6529;
(b) E. Bustelo, J.J. Carbò, A. Lledòs, K. Mereiter, M.C. Puerta, P. Valerga, J. Am. Chem. Soc. 125 (2003) 3311.
[45] (a) J.L. Speier, Adv. Organomet. Chem. 17 (1979) 407;
(b) J.L. Speier, J.A. Webster, G.H. Barnes, J. Am. Chem. Soc. 79 (1957) 974.
[46] J.F. Harrod, A.J. Chalk, in: I. Wender, P. Pino (Eds.), Organic Synthesis Via Metal Carbonyls, vol. 2, Wiley, New York, 1977, p. 673, and references therein.
[47] A.L. Prignato, W.C. Trogler, J. Am. Chem. Soc. 109 (1987) 3586.
[48] (a) S. Sakaki, N. Mizoe, M. Sugimoto, Organometallics 17 (1998) 2510;
(b) S. Sakaki, W. Ogawa, M. Kinoshita, J. Phys. Chem. 99 (1995) 9933;
(c) S. Sakaki, M. Ieki, J. Am. Chem. Soc. 115 (1993) 2373.